Energy & Environmental Science

Cite this: DOI: 10.1039/c2ee21463f

www.rsc.org/ees

PAPER

Impact of Sr segregation on the electronic structure and oxygen reduction activity of $SrTi_{1-x}Fe_xO_3$ surfaces†

Yan Chen,[a] WooChul Jung,‡[b] Zhuhua Cai,[a] Jae Jin Kim,[b] Harry L. Tuller[b] and Bilge Yildiz*[a]

Received 23rd February 2012, Accepted 2nd April 2012
DOI: 10.1039/c2ee21463f

The correlation between the surface chemistry and electronic structure is studied for $SrTi_{1-x}Fe_xO_3$ (STF), as a model perovskite system, to explain the impact of Sr segregation on the oxygen reduction activity of cathodes in solid oxide fuel cells. Dense thin films of $SrTi_{0.95}Fe_{0.05}O_3$ (STF5), $SrTi_{0.65}Fe_{0.35}O_3$ (STF35) and $SrFeO_3$ (STF100) were investigated using a coordinated combination of surface probes. Composition, chemical binding, and valence band structure analysis using angle-resolved X-ray photoelectron spectroscopy showed that Sr enrichment increases on the STF film surfaces with increasing Fe content. *In situ* scanning tunnelling microscopy/spectroscopy results proved the important and detrimental impact of this cation segregation on the surface electronic structure at high temperature and in an oxygen environment. While no apparent band gap was found on the STF5 surface due to defect states at 345 °C and 10^{-3} mbar of oxygen, the surface band gap increased with Fe content, 2.5 ± 0.5 eV for STF35 and 3.6 ± 0.6 eV for STF100, driven by a down-shift in energy of the valence band. This trend is opposite to the dependence of the bulk STF band gap on the Fe fraction, and is attributed to the formation of a Sr-rich surface phase in the form of SrO_x on the basis of the measured surface band structure. The results demonstrate that Sr segregation on STF can deteriorate oxygen reduction kinetics through two mechanisms – inhibition of electron transfer from bulk STF to oxygen species adsorbing onto the surface and the smaller concentration of oxygen vacancies available on the surface for incorporating oxygen into the lattice.

[a]*Laboratory for Electrochemical Interfaces, Department of Nuclear Science and Engineering, Massachusetts Institute of Technology, Cambridge, MA 02139, USA. E-mail: byildiz@mit.edu; Fax: +1 617-258-8863; Tel: +1 617-324-4009*
[b]*Department of Materials Science and Engineering, Massachusetts Institute of Technology, Cambridge, MA 02139, USA*

† Electronic supplementary information (ESI) available. See DOI: 10.1039/c2ee21463f

‡ Present address: Department of Materials Science, California Institute of Technology, Pasadena, CA 91125, USA.

1. Introduction

Because of their high efficiency and fuel flexibility, solid oxide fuel cells (SOFCs) offer the potential to contribute significantly to a clean energy infrastructure.[1,2] However, their high working temperatures (>800 °C) impose challenges due to accelerated materials degradation and high cost. The lowering of the working temperature has, therefore, become a strong focus of

Broader context

The high efficiency and fuel flexibility of Solid Oxide Fuel Cells (SOFCs) are enabled by their relatively high working temperatures at 800 °C or above. These high temperatures, on the other hand, introduce challenges related to material stability and cost. In order to decrease the SOFC working temperature to an intermediate range (~500 to 700 °C), new cathode materials with high activity to oxygen reduction reaction (ORR) are needed. To rationally develop novel and highly active cathode materials, a deeper understanding of the correlation between the cathode surface chemistry, electronic structure and ORR activity is necessary. Surface electronic structure is a key indicator to charge transfer kinetics on the cathode, which is a critical step in the oxygen reduction process. Furthermore, it is known that the surface chemistry and structure of perovskite type oxide cathodes deviate from their bulk. Because of the harsh working conditions of SOFCs (high temperatures and reactive gas environments), it has been a formidable challenge to obtain surface electronic structure information *in situ* and fundamentally relate this information to the ORR activity. This paper contributes to advancing our fundamental understanding of the correlation between surface chemical inhomogeneities, electronic structure and ORR activity by using novel *in situ* scanning probe methods. Our scientific findings are expected to provide guidelines for the development of high performance cathode materials.

research.[3] At reduced temperatures (<700 °C), slow Oxygen Reduction Reaction (ORR) kinetics at the cathode become a major barrier to the implementation of high performance SOFCs. To rationally design new cathode materials with high ORR activity, it is necessary to understand the governing ORR mechanisms and identify key descriptors of the cathode materials that directly control ORR activity. The strength of oxygen adsorption and the energy barriers to oxygen dissociation, reduction and incorporation are believed to be the processes that determine oxygen reduction activity on perovskite oxides.[4,5]

The energetics of these processes depends, in part, on the cathode electronic structure. In transition metal catalysis, the d-band structure[6] is a well-established descriptor of ORR activity. However, the applicability of the d-band model to perovskite oxide SOFC cathodes is limited by their complex surface chemistry (an anion and two cation sublattices), the role of oxygen vacancies in surface activity,[7,8] and the deviations of surface structure and chemistry due to cation segregation.[9–12] Recent computational and experimental studies have attempted to develop new fundamental descriptors of surface reactivity to ORR on perovskite oxides. Key descriptors include the e_g-state occupancy and the covalency of the transition metal–oxygen bond[13] for low-temperature ORR activity in water, and the O 2p band center energy[14] and the minority electronic carrier density in the conduction band of the material[15] for high temperature ORR activity. While all these efforts demonstrate the essential role of electronic structure in ORR, they focus on the bulk electronic structure, which is easier to quantify both experimentally and computationally. The general applicability of these more recent models is also limited because of the deviations from nominal composition, structure and phase as a result of cation segregation and/or lattice reconstruction on the surfaces of oxide cathodes.

The surface structure and chemistry (*i.e.*, cation concentration and oxygen non-stoichiometry) are dynamically driven by the surrounding harsh environment at high temperatures, oxygen partial pressures and electrochemical potentials.[9–11,16–19] As a result, the surface can become quite a "different material" than the bulk phase. Cation segregation is now a commonly observed and acknowledged phenomenon on the surface of SOFC cathode materials, such as on $SrTiO_3$ (STO),[9] (La,Sr)MnO_3 (LSM)[10–12] and $SrTi_{1-x}Fe_xO_3$ (STF).[18] Such deviations from the bulk nominal composition and phase can directly alter the surface electronic structure. For example Liang and Bonnell[20] showed that the segregated Sr-rich islands that form on annealed single-crystal STO surfaces differ from the un-segregated surface both in atomic and in electronic structure. A much wider band gap (nearly 6 eV) was found on the Sr-rich segregate islands compared to that on the un-segregated pristine surface (3.2 eV). Direct evidence for modified valence and conduction band structures of segregated surfaces under various conditions was also reported for $SrFeO_3$,[21] LSM,[22] STO[23,24] and (La,A)MnO_3 (A = Ca, Sr, Ba).[25]

Despite the wide-ranging observations on cation segregation on perovskite-type oxides, the answer to how such surface segregation layers influence the oxygen reduction kinetics remains controversial. Taking Sr segregation as an example, it has been reported that Sr segregation on the surface leads to the degradation of oxygen reduction activities on (La,Sr)CoO_3 (LSC),[26] LSM[27] and STF.[18] In contrast to these results, other groups have observed the enhancement of oxygen exchange kinetics by purposefully decorating (*via* deposition) SrO onto the surface of LSC[28] and Fe-doped STO.[29] However, the physical origin behind these empirical observations is not understood.

It is clear from the interesting evidence summarized above that cathode surface chemistries can markedly vary, and that the atomic structure of the segregated surface is important in determining the ORR activity. An important motivating point for this paper is the lack of understanding of how the surface structure, in the presence of thus-far inevitable segregation of cations, affects the ORR activity. The specific open questions of importance here are: (1) what are the non-bulk-like structures that form on these segregated perovskite oxide surfaces at elevated temperatures? (2) How is the electronic structure affected by the formation of a new surface composition and structure? (3) How does the segregated surface electronic structure affect the ORR activity of the cathode? Our goal is to contribute to answering these questions by using the model cathode material system STF.

In this paper, we identify the surface chemistry and electronic structure of the STF system as a function of Fe content and then discuss our results in the context of existing models that correlate surface electronic structure to oxygen reduction activity. A unique tool used in this study is *in situ* scanning tunnelling microscopy/spectroscopy (STM/STS) to probe the surface morphology and electronic structure at high temperature and in oxygen environments. Angle-resolved X-ray photoelectron spectroscopy (AR-XPS) is used to obtain the chemical composition at different depths from the surface. While STS provides the surface electronic structure with high spatial resolution, AR-XPS provides information about the valence band structure in a laterally averaged way but at different depths from the surface. STF is a promising cathode material[30–32] whose ionic and electronic conductivities can be adjusted over wide limits with variations in the Fe concentration at the B-site (B in ABO_3), making it a good model system for our study. Its bulk defect chemistry and bulk electronic structure have been well studied.[30,33,34] More importantly, the oxygen exchange process at the STF surface is shown to be the rate limiting step in the overall ORR kinetics of the cathode.[31,32] In the recent report by Jung and Tuller, Sr excess was found on the STF surfaces and was correlated with a strong degradation of oxygen reduction kinetics on the cathode.[18] Such a Sr excess phase could be in the form of SrO, $SrCO_3$, $Sr(OH)_2$ or Ruddlesden Popper (RP) $SrO{\cdot}n$Sr(Ti,Fe)O_3. While in ref. 18 the surface segregation layer was thought to be SrO or $SrO{\cdot}n$Sr(Ti,Fe)O_3, the exact nature of the surface atomic structure and its influence on the surface electronic structure have not been clarified to date. In this study, by combining surface chemical results from AR-XPS and surface band structure results from STS, we provide further evidence that such a Sr-excess phase on the STF surface is more likely to be in the form of SrO. The mechanism of the degradation of ORR activity due to Sr excess on the surface is discussed on the basis of the changes in the measured surface electronic structure.

2. Experimental

Three compositions, STF5, STF35 and STF100, in dense thin film form of 20 nm thickness, were prepared by pulsed laser deposition (PLD) on single crystal (100) oriented yttria stabilized

zirconia (YSZ) substrates (MTI Corporation, Richmond, CA). High resolution X-ray Diffraction (XRD) was used to confirm that all the films were highly textured in the (110) out-of-plane orientation, as shown in ESI, Fig. S1†. A modified variable-temperature scanning tunnelling microscope (VT-STM) (Omicron GmbH, Tanusstein, Germany) was used to image the surface morphology and to obtain surface electronic structure information with high spatial resolution at elevated temperatures (up to 430 °C) and in oxygen gas pressures (10^{-3} mbar). STM was performed in constant-current mode using Pt/Ir tips made by chemical etching. A tip bias voltage of 2 V and feedback tunnelling current of 50–500 pA were used. A retractable oxygen doser placed near the STM stage in the chamber was used to directly expose the sample to oxygen during the STM/STS measurements. A pyrolytic boron nitride (PBN) heater was used for sample cleaning and for the *in situ* STM/STS measurements at elevated temperatures.

An Omicron EA 125 hemispherical analyzer and an Omicron DAR 400 Mg/Al dual anode non-monochromated X-ray source were used for the XPS measurements. These measurements were performed in the same ultra-high vacuum (UHV) chamber to which the VT-STM is connected. An Al K X-ray source (1486.7 eV) operated at 300 W was used for all the XPS data shown in this paper. Peak-fitting and chemical quantification were performed using the CasaXPS 2.3.15 software. Sr 3d, Ti 2p and Fe 2p spectra were used to assess the chemical composition on the STF surface. Information from different depths was acquired by changing the emission angle from 0° to 80° as defined relative to the surface normal plane. The sampling depth at 0° is about 5 nm for Fe 2p, 6 nm for Ti 2p and 7 nm for Sr 3d.[35] By increasing the emission angle to 80°, the sampling depths decrease to 17% of those at 0°. The surfaces of the thin-film STF samples were cleaned by low energy Ar sputtering (0.5 keV) for 4 minutes followed by heating in oxygen at 450 °C at pressures of 10^{-5} to 10^{-3} mbar to remove water- and carbon-related adsorbates on the surface due to air exposure after film growth. All STM, STS, and XPS results reported here were obtained after the cleaning procedure.

3. Results and discussion

3.1 Morphology

Fig. 1 shows the STM images obtained at 345 °C, $P_{O2} \approx 1 \times 10^{-3}$ mbar for STF samples with differing Fe content. The surface morphology was found to be consistent among all samples, irrespective of the Fe content. Samples are polycrystalline ((110) textured) with grain sizes on the order of 10–30 nm. The surface roughness of each film is less than 1 nm.

3.2 Surface chemical composition and the binding environment of Sr

The photoelectron spectra of each constituent cation on the STF films measured by AR-XPS are shown in Fig. 2. Here we assess both the relative enrichment of the Sr cation (Fig. 3(a)) and the chemical environment of Sr that exist on the surface (Fig. 2(a) and 3(b)).

First, we use $Sr/(Ti + Fe)_{0°}$ and $Sr/(Ti + Fe)_{80°}$ to refer to the ratio of the A-site cation content to the B-site cation content measured at emission angles of 0° (more bulk sensitive) and 80° (more surface sensitive), respectively. We assess the $[Sr/(Ti + Fe)_{0°}]/[Sr/(Ti + Fe)_{80°}]$ ratio to represent the relative Sr enrichment at the surface, rather than comparing the absolute value of the Sr content at the 0° and 80° emission angles. This eliminates the effect of uncertainties in the quantitative analysis arising from the variations in the detection depth and sensitivity factors for different elements. $[Sr/(Ti + Fe)_{80°}]/[Sr/(Ti + Fe)_{0°}]$ was found to increase on the STF films with increasing Fe content (Fig. 3 (a)). The Fe/(Ti + Fe) on/near the surface of each sample was found close to the bulk stoichiometric content. Such a Sr segregation on the surface of STF films could be associated with the formation and separation of surface-localized Sr-enriched phases, such as the RP phase $SrO \cdot nSr(Ti,Fe)O_3$ (ref. 36–39) or SrO[20] as also suggested in ref. 18. We offer two possible explanations for the increased segregation of Sr onto STF films with increasing Fe content. First is the chemical (electrostatic) driving force, due to the existence of a space charge layer (excess oxygen vacancies that are positively charged) in the near surface and surface polarization.[40,41] An increase in Fe content may make it easier to equilibrate a larger amount of (positively charged) oxygen vacancies near the surface that electrostatically prefers Sr^{2+} ions more than the Ti^{4+} or $Fe^{3+/4+}$ ions. Second is the elastic interactions related to the large size of Sr, which can drive the Sr to free surfaces to minimize the elastic energy of the system[42,43] (note that the lattice parameter of STF decreases with increasing Fe content[18]). In the authors' ongoing research, these driving forces for the cation segregation phenomenon are being assessed quantitatively using both experiments and computation.

To deduce the chemical binding environment of the Sr-rich surface layer, we assess the photoelectron spectra from the

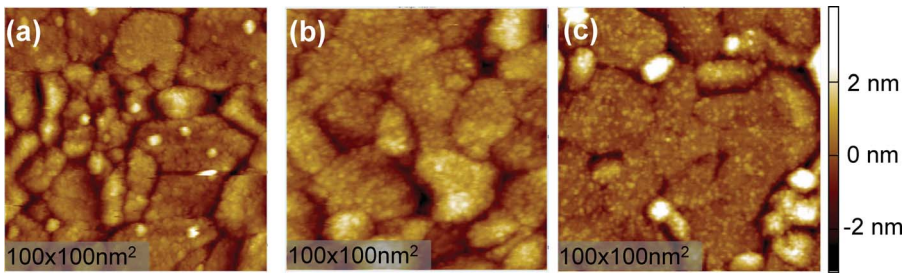

Fig. 1 Surface structure of 20 nm thick (a) $SrTi_{0.95}Fe_{0.05}O_3$ (STF5), (b) $SrTi_{0.65}Fe_{0.35}O_3$ (STF35) and (c) $SrFeO_3$ (STF100) films, imaged by scanning tunnelling microscopy (STM) at 345 °C and 1×10^{-3} mbar oxygen pressure.

constituent elements. The Sr 3d peak was found to be markedly different at the surface ($\theta = 80°$) compared to its signature from the bulk ($\theta = 0°$) of the material (Fig. 2(a)). In order to identify the contribution from these two different binding environments, the Sr 3d spectra were deconvoluted with two sets of spin–orbit split doublets, at a fixed separation of 1.75 eV and an area ratio of 2 : 3. The doublet shown in green in Fig. 2(a) is located at about 1.1 eV higher binding energy compared to the main Sr 3d doublet shown in red, at both $\theta = 0°$ and $\theta = 80°$. The intensity of the doublet at the higher binding energy increases when the photoelectron emission angle changes from 0° to 80°, confirming that it originates from the surface. We refer to the main Sr 3d doublet as $Sr_{lattice}$, and to the higher-binding energy Sr species as $Sr_{non\text{-}lattice}$. The $Sr_{non\text{-}lattice}$ could potentially arise from the Sr–OH,[44,45] Sr–CO_3,[24] under-coordinated Sr cations,[46] or some combination of these three. At 80° emission angle, the –CO_3 content is not detectable for STF5, while it is 2% and 9% in STF35 and STF100 samples. These results indicate that, for STF5, the $Sr_{non\text{-}lattice}$ arises only from Sr–OH and/or undercoordinated Sr cations, and for STF35 and STF100, $Sr_{non\text{-}lattice}$ may also contain a small amount of additional Sr–CO_3 on the top 1 nm layer.

The $Sr_{non\text{-}lattice}/Sr_{lattice}$ serves as another indication of the extent of Sr surface segregation and/or phase separation. Sr–OH and Sr–CO_3 as secondary binding environments or phases, reflected here in the $Sr_{non\text{-}lattice}$ peak, are known to form more readily on SrO when the sample is exposed to air[45,47] after deposition (and may be difficult to eliminate entirely during the *in situ* cleaning procedure prior to analysis). Therefore, the $Sr_{non\text{-}lattice}/Sr_{lattice}$ could indirectly represent the extent of SrO separation on the surface of STF films. The increase in the $Sr_{non\text{-}lattice}/Sr_{lattice}$ (Fig. 2(a) and 3(b)) confirms that Sr segregates/separates more on the surface of the STF films with higher Fe content. Fig. 3(b) shows that, at 80° (within ~1 nm detection depth), the increase in the $Sr_{non\text{-}lattice}/Sr_{lattice}$ from STF5 to STF35 is much larger than that at 0° (within ~7 nm detection depth), and such an increase reaches saturation when the Fe content further increases from 35% to 100%. This fact indicates that, although the extent of the total surface Sr segregation and separation is more pronounced for STF100 compared to STF35 (Fig. 3a) in their near-surface regions, the Sr chemical environment is very similar at the top-most layers on these two compositions. From this, we deduce that the STF35 and STF100 surfaces are terminated by a similar, thin SrO_x layer. (We use x here to denote the potentially defective or non-stoichiometric structure of this surface SrO phase, separated on STF.) We provide more evidence for the formation of the SrO phase on STF surfaces from the electronic structure measurements shown in Section 3.3. Furthermore, we discuss the important role of this phase in the context of surface ORR activity of STF in Section 3.4.

On the other hand, the Fe 2p spectra shapes are very similar on the surface (80°) and in the bulk (0°), as shown in Fig. 2(b) and S2, ESI†. There is no detectable difference between the Ti 2p spectra from bulk to surface for STF5. The Ti 2p spectra on the surface of STF35 are slightly broader than the bulk (about 0.3 eV larger in FWHM), which may be due to the variation of the chemical environment induced by Sr segregation.

3.3 Surface electronic structure

3.3.1 Energy gap probed by *in situ* STS. The surface electronic structure of each of the STF thin films was probed using STS at high temperature (up to 430 °C) and in oxygen environment (at 10^{-3} mbar). At room temperature, the STF films were too insulating to permit STM/STS measurements. The ability to heat the sample *in situ* enabled us to study the surface morphology and electronic structure by STM/STS. A reference tunnelling spectrum on a single crystal 0.05% Fe doped $SrTiO_3$ surface from this work, showing the signature of the $SrTiO_3$ band gap with defect states, is presented in the ESI, Fig. S3†. At 345 °C, STF35 and STF100 surfaces were found to exhibit an

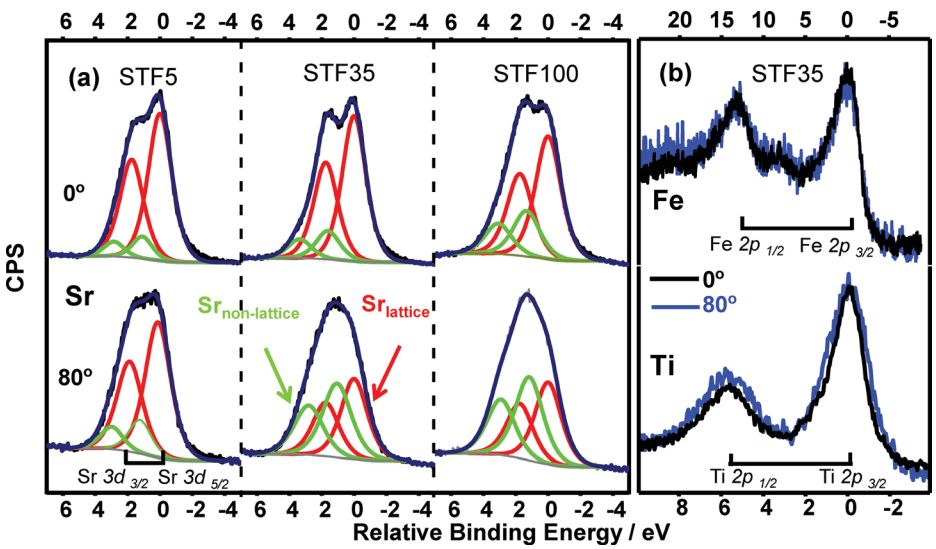

Fig. 2 (a) Comparison of the Sr 3d spectra on STF5, STF35 and STF100 at emission angles of 0° and 80°. The red doublets correspond to the bulk-coordinated $Sr_{lattice}$ and the green doublets are attributed to the binding environment on the surface $Sr_{non\text{-}lattice}$. The binding energy of the Sr spectra was referenced to the peak position of the $3d_{5/2}$ peak in the main doublet ($Sr_{lattice}$) for comparison. (b) Comparison of the Fe 2p and Ti 2p spectra of STF35 at emission angles of 0° and 80°. The binding energies on the Fe spectra and Ti spectra were referenced to Fe $2p_{3/2}$ and Ti $2p_{3/2}$, respectively.

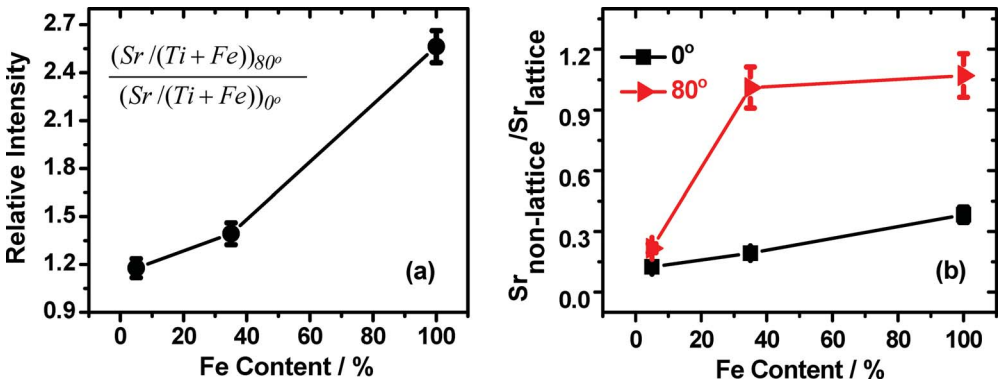

Fig. 3 (a) Comparison of the relative Sr enrichment on the surface of STF thin films with varying Fe content. (b) The ratio of Sr in the non-lattice phase to Sr in the lattice phase (as shown in Fig. 2) on the surface ($\theta = 80°$) and in the bulk ($\theta = 0°$) in STF5, STF35 and STF100.

energy gap (E_g) between the valence band (VB) and conduction band (CB) as shown in the tip bias *vs.* tunnelling current plot in Fig. 4(a), and in the distribution of VB top and CB bottom in Fig. 4(c). On the other hand, no apparent energy gap was present on the STF5 surface under the same conditions. The absence of a band gap for the STF5 surface is associated with the defect states that are created within the forbidden region when the sample is heated to high temperature. These newly created gap states arise from the formation of oxygen vacancies that modify the d band structure of neighbouring transition metal ions.[48–51] Despite the moderate oxygen pressures in the analysis chamber, the environment was still potentially reducing enough for oxygen vacancies to form near the surface during the high-temperature tunnelling spectroscopy measurements. The lack of a measurable surface band gap was also observed in the room-temperature tunnelling spectroscopy measurements on STO after it was reduced by heating in UHV at high temperature.[52,53] Furthermore, a similar disappearance of the surface energy gap at high temperatures (up to 580 °C in oxygen partial pressure) has been observed in two other perovskite oxides, LSM and LSC, by *in situ* STM/STS measurements[17,51,54] and the reason is the same as here. While more oxygen vacancies in STF are expected with increasing Fe content (and thus, defect states that may lead to a metallic-like signature in the tunnelling spectrum with no gap), the large energy gap on the surface of STF35 and STF100 is attributed to a surface phase that behaves differently from the bulk STF phase. Further increasing the temperature from 345 °C to 430 °C decreases the band gap on STF35, shown in Fig. 5(a). Both the bottom of the conduction band and the top of the valence band shift towards the Fermi level. This result confirms that heating the STF films introduces new surface states in the gap, with increasing state density for higher temperatures.

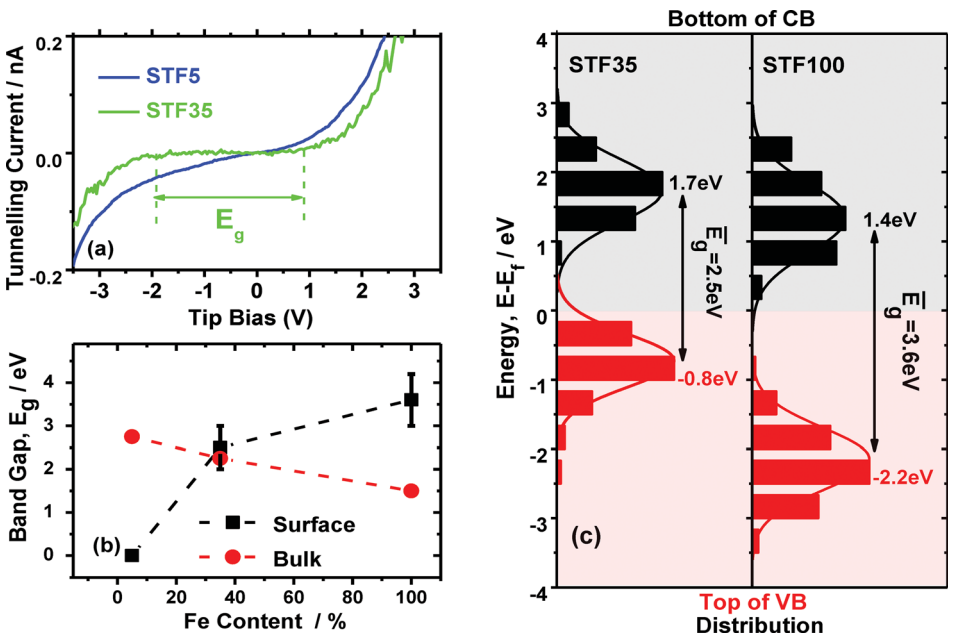

Fig. 4 (a) Representative tunnelling spectra on the STF5 and STF35 surfaces, showing the lack and the presence of a band gap, E_g, respectively. (b) Comparison of the band gap at the surface (black squares) measured by scanning tunnelling spectroscopy (STS) in this work and in the bulk (red circles) for STF5, STF35 and STF100. The "Bulk" values are taken from ref. 30. (c) Distribution of the band edges, the top of the valence band (in red) and the bottom of the conduction band (in black), for STF35 and STF100. All surface STS measurements reported in (a)–(c) are at $P_{O2} \approx 1 \times 10^{-3}$ mbar and 345 °C.

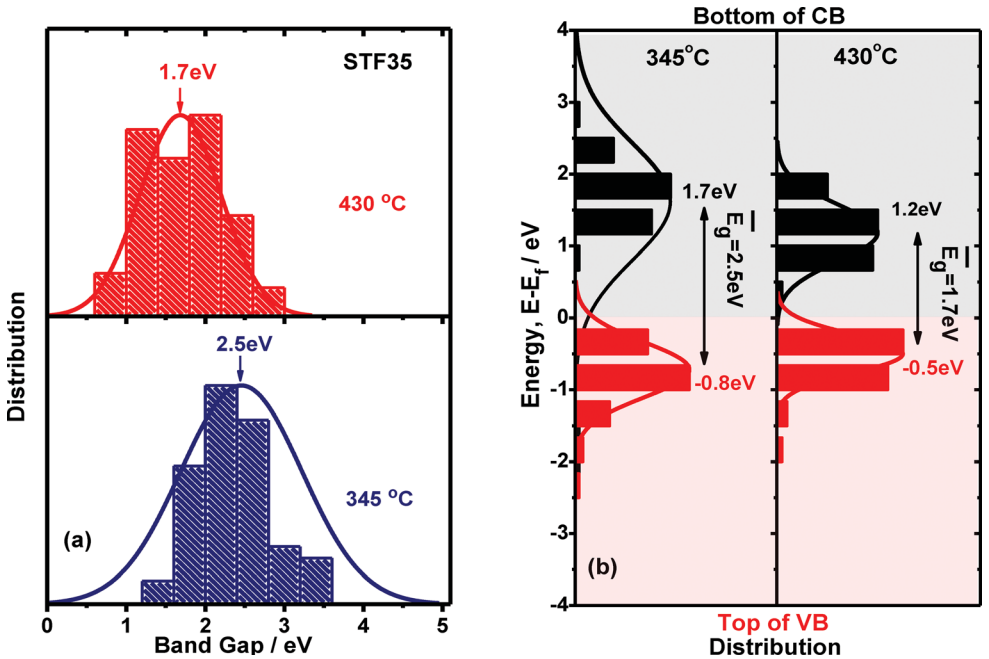

Fig. 5 (a) Comparison of the surface band gap, E_g, at the surface of STF35 measured by scanning tunnelling spectroscopy at $P_{O2} \approx 1 \times 10^{-3}$ mbar and two different temperatures of 345 °C and 430 °C. (b) Distribution of band edges, the top of the valence band (in red) and the bottom of the conduction band (in black), for STF35 under the same conditions as in (a).

Importantly, we note that the band gap on STF100 is on average larger than the band gap on STF35 (Fig. 4(b) and (c)). This trend of increasing energy gap from STF5 to STF35 to STF100 is opposite to the Fe-dependence of the bulk band gap in STF.[30,34] The top of the valence band in the STF system consists mainly of the Fe 3d and O 2p states, while the bottom of the conduction band is assigned to the Ti 3d states.[30,34] Increasing the Fe content leads to greater overlap between Fe states or between Fe and oxygen states, resulting in the increase in state density of Fe-derived bands. Hence in bulk STF, the valence band is expected to shift up towards the conduction band as a function of increasing Fe content. However, as apparent from Fig. 4(c), one observes that the valence band moves away from the conduction band (and away from the Fermi level) when the Fe content increases from 35% to 100%. This observation strongly suggests that the surface differs from the STF phase composing the underlying film.

The two possible Sr excess phases on the surface, SrO and RP, are known to have larger band gaps than the STF perovskite phase.[55,56] The coverage of such an insulating layer blocks the tunnelling of electrons from the STF bulk states and results in the occurrence of a larger band gap at the surface compared to the bulk. The magnitude of the surface band gap can indicate the identity of the surface phase. To identify which phase, SrO or RP, is more likely to exist on the surface of these STF films, we compare the band gap values of the RP series ($SrO \cdot n SrTi_{1-x}Fe_xO_3$) as a function of n and x (Table 1). The band gap in the RP phases decreases with increasing n due to the increase of symmetry in the structure:[56] largest for $n = 1$ and smallest for the perovskite where $n = \infty$. The band gap of the STF100 film surface measured in this work ranges from 3.0 to 4.2 eV with a mean value of 3.6 eV at 345 °C and oxygen pressure of 10^{-3} mbar. This value is much larger than the largest band gap value in the RP series $SrO \cdot n SrFeO_3$, that is about 1.0 eV[57,58] for Sr_2FeO_4 ($n = 1$). Considering the fact the band gap value of SrO (~5.5 to 6 eV)[20,55] is closer to our results, it is more likely that the Sr segregated phase on the STF100 surface is SrO instead of $SrO \cdot n Sr(Ti,Fe)O_3$. In addition, if the surface were forming an RP structure, the increase of Fe content in it should have decreased its band gap[30,57] (as shown in Table 1), but this is again opposite to the trend that we found for the measured surface band gap with Fe content (Fig. 4(b)). This observation further supports our argument that the Sr segregation layer is more likely to be SrO rather than $SrO \cdot n Sr(Ti,Fe)O_3$.

To confirm and elucidate the origin of these surprising results regarding the electronic structure measured at the surface of our STF films (opposite to that of the bulk electronic structure reported in the literature), we studied the valence spectra with AR-XPS, as discussed in the next section.

Lastly, because STS can be performed with high spatial resolution on the sample surface in coordination with STM, we can

Table 1 Comparison of the band gap, E_g, of the Ruddlesden–Popper phase, $SrO \cdot n SrTi_{1-x}Fe_xO_3$, with varying n and x. In contrast to these values, the E_g of SrO is 5.5–6 eV[20,55]

E_g decreases with x ↓ / E_g decreases with n →	n = 1	n = ∞
x = 0	Sr_2TiO_4 3.8 eV [57]	$SrTiO_3$ 3.2 eV [20]
x = 1	Sr_2FeO_4 0.8-1.0 eV [57,58]	$SrFeO_3$ 0 eV [21,56 a]

[a] This E_g value for $SrFeO_3$ does not consider the contribution of oxygen non-stoichiometry.

deduce whether the variation of the energy gap is correlated with the surface morphology. Fig. 4(c) shows the distribution of band edge positions probed and sampled by STS on STF35 and STF100 sample surfaces. Such a scatter in electronic structure is likely associated with various heterogeneities in the form of local structure, composition, strain fields or defects like surface oxygen vacancies. A clear correlation between the extent of the band gap distribution and evident structural features (*e.g.* grain boundaries) on the surface of these STF films was not found in our study, as shown in Fig. S4 of ESI†.

3.3.2 Valence band structure probed by XPS. As shown in Section 3.3.1, the increase in the energy gap on the STF surface with increasing Fe content was largely attributed to changes in the valence band edge observed in our STS measurements. AR-XPS was used here to deduce laterally averaged information about the valence band structure on STF films at different depths from the surface. Fig. 6 shows the valence band of the STF100 film at emission angles of 0°, 60° and 80° (corresponding to probed depths of about 7 nm, 3 nm and 1 nm, respectively, using the electron kinetic energies in the valence band region[35]). All the binding energies shown in Fig. 6 are with reference to the Sr 4p peak position (at 19.4 eV for STO) as ref. 24. When the emission angle increases from 0° (bulk) to 80° (near-surface), an extra peak appears at about 11 eV in the O 2p region of the valence band on STF100. We recall that STF100 has the greatest extent of Sr enrichment at/near the surface (Fig. 2(a)). For STF5 and STF35, there is no noticeable difference between 0° and 80°, indicating that only for STF100 is the valence structure markedly different at the surface compared to the bulk. If the same is true of STF5 and/or STF35 samples, it means that the segregation layer is not thick enough to cause a noticeable change in valence spectra on the surface of STF5 and STF35 in our measurement system. This additional state, deeper in the valence band on the surface of STF100, is consistent with our STS measurements discussed in Section 3.3.1 – that is the presence of a larger band gap on STF100 compared to that on STF35, driven by the downshift of the top of the valence band.

This surface phase that alters the surface electronic structure (evidently the valence band top) can be interpreted by comparing our AR-XPS results to previous studies of the correlation between Sr segregation and valence band structure.[21–24] de Jong *et al.*'s work[22] on LSM, using XPS and ultraviolet photoelectron spectroscopy (UPS), showed that the additional O 2p peaks at higher binding energies in the valence band arose from the SrO or $SrCO_3$ segregation layer at the surface. Bocquet *et al.* also compared XPS and UPS results and identified a residual phase at around 9 eV, which is most likely to be SrO on the surface of near-stoichiometric $SrFeO_3$.[21] SrO segregation layers on $SrTiO_3$ were also found to change the valence band structure on the surface in other studies using XPS, UPS and metastable impact electron spectroscopy.[23,24] Thus, we conclude that the Sr segregation layer in the form of SrO on the surface of STF100 is the reason for the additional state located deeper in the valence band (in O 2p). This result is consistent with the conclusion we obtained about the formation of a SrO phase on the STF surfaces in Section 3.3.1. The downshift of the O 2p band relative to the Fermi level at the surface, due to the SrO_x segregation layer, is expected to inhibit the oxygen surface exchange, as discussed in the next section.

3.4 Effect of Sr surface segregation on oxygen reduction activity

The STS and AR-XPS results demonstrate that Sr segregation on STF surfaces alters the electronic structure significantly compared to the bulk behaviour. Here we discuss how these findings mechanistically relate to the oxygen reduction kinetics on STF surfaces. We recall that charge transfer during oxygen exchange on the STF surface can be the rate determining ORR step once the bulk electronic and ionic conductivities are sufficiently high. In the work of De Souza and Kilner,[7,59] the availability of electronic species was reported to play an essential role in the oxygen exchange processes in mixed ionic conductors. Recently Jung and Tuller[15] also showed that enhancements in the bulk electronic and ionic conductivity, beyond certain values,

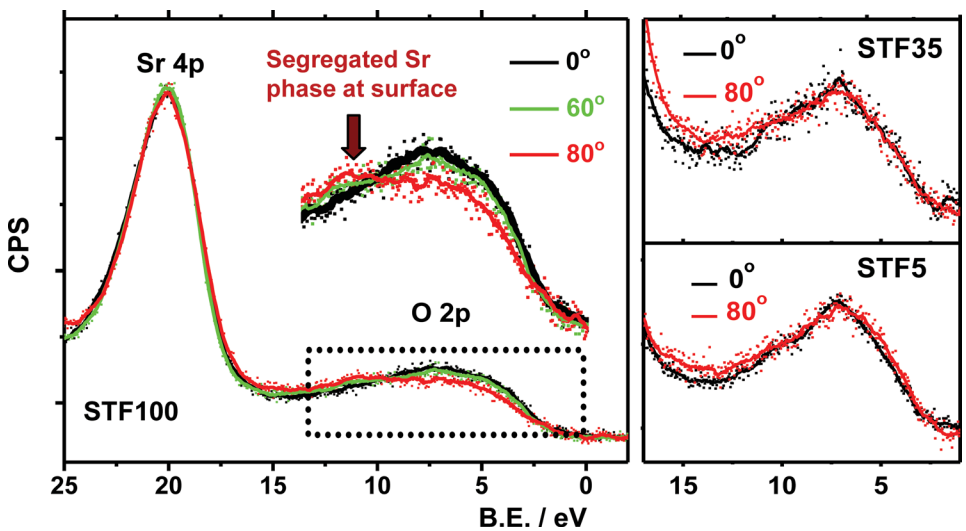

Fig. 6 Valence band structure obtained by angle-resolved X-ray photoelectron spectroscopy on STF100, STF35 and STF5 at different detection angles.

have little impact on the oxygen reduction kinetics of STF. Instead, the key factor governing oxygen exchange at the surface was found to be the availability of electrons, the minority electronic species in bulk STF. Several successive reaction steps involving electron transfer are likely to take place during oxygen exchange on the surface:

$$O_{2\_ads} \rightarrow 2O_{ads};\ 2O_{ads} + 2e^{/} \rightarrow 2O_{ads}^{-} \text{ or}$$

$$O_{2\_ads} + 2e^{/} \rightarrow O_{2ads}^{2-} \rightarrow 2O_{ads}^{-} \quad (1)$$

$$O_{ads}^{-} + V_O^{\cdot\cdot} + e^{/} \rightarrow O_o^{x} \quad (2)$$

The first involves electron transfer to the adsorbing oxygen in the form of either dissociated O or molecular O_2. The second describes electron transfer during incorporation of oxygen into the lattice assisted by the presence of an oxygen vacancy.

As shown in the previous sections, Sr-segregation on STF film surfaces results in a surface with a larger band gap compared to the bulk. The insulating nature of this segregated layer may serve as a barrier to electron transfer from the bulk phase to the reacting oxygen species on the surface. Hence a decrease in the ORR activity of the STF material as a cathode would be expected. Indeed, in Jung and Tuller's previous report, the surface oxygen exchange rate was found to increase with Fe content, as shown in Fig. 7(a),[15] and was shown to correlate to the availability of electrons in the conduction band of STF as minority carriers. However, such an increase is rather suppressed at higher Fe levels compared to the large increases in the ionic and electronic conductivity. This effect is observed by the small difference in k while going from STF35 to STF100 in Fig. 7(a). The similarity of the surface chemistry on these two films with Sr-segregation (*i.e.* the relative $Sr_{non\text{-}lattice}$ amount as shown in Fig. 3(b)) is consistent with this behavior. Removing the Sr-enriched segregation layer through chemical etching was shown to markedly improve the surface exchange kinetics on STF by almost one order of magnitude (as shown in Fig. 7(b) for STF100).[18] Upon etching STF35 and STF100 (using 0.14 mol l^{-1} HCl for 10 s) and examining their surfaces by XPS and STS, we found a decrease in the surface Sr/(Ti + Fe) ratio as shown in Fig. 7(c) and a corresponding decrease in the apparent band gap as shown in Fig. 7(d). For example, the band gap on the STF100 surface decreases from ~3.6 eV to ~2.8 eV following the etching of the segregation layer. This is again consistent with our earlier observations showing the correlation of an increased band gap with increased segregation of a Sr-rich segregated phase to the surface. Thus, one possible mechanism by which the STF surface inhibits oxygen reduction at large Fe levels is by the formation of a separate SrO_x layer serving as a barrier layer that inhibits electron transfer from bulk STF to the adsorbing oxygen species. This is schematically illustrated in Fig. 8(a). Whether such a blocking layer partially or fully covers the cathode surface area depends on the extent of segregation. We are currently probing the spatial extent of this coverage by using other surface sensitive measurement techniques, *i.e.*, low energy ion scattering.

Another possible mechanism is related to the consequences of the downshift of O 2p states in the valence band shown in

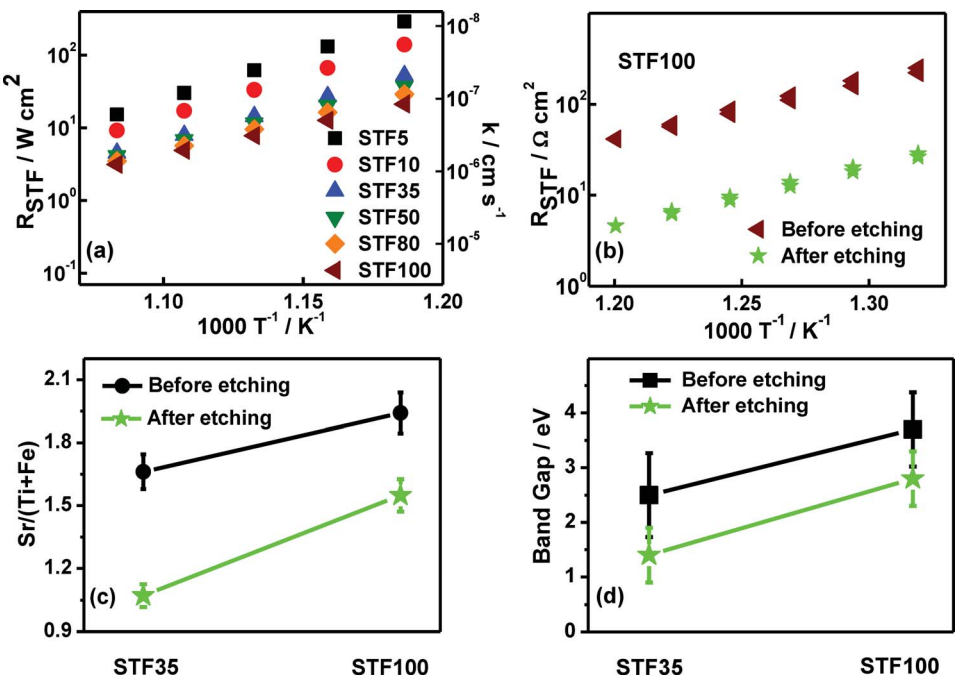

Fig. 7 (a) Temperature dependence of the area specific resistance (R_{STF}) and surface exchange coefficient (k) for STF thin film electrodes. (b) R_{STF} for STF100 is shown both before and after chemical etching to remove Sr excess phase. ((a) and (b) are reproduced with permission from ref. 15 and 18.) (c) Comparison of the ratio of A site to B site cations, Sr/(Fe + Ti) quantified from XPS, for STF35 and STF100 before and after HCl etching. (d) Comparison of the band gaps measured by STS for STF35 and STF100 before and after HCl etching.

our STS and AR-XPS results. From the valence spectra in Fig. 6, the center position of the O 2p band shifts down by about 2 eV relative to the Fermi level. Lee *et al.*[14] recently demonstrated that the bulk O 2p band position relative to the Fermi level (E_f) has a direct linear correlation with the oxygen exchange rate at the surface for perovskite oxides. Such a correlation is due to the key role of the stability of the oxygen sub-lattice in the ORR kinetics. The closer the O 2p band is to E_f, the more unstable the oxygen sub-lattice is. Consequently more oxygen vacancies can be accommodated to assist the surface incorporation of oxygen. In our case, the downshift of the O 2p state relative to E_f on the STF100 surface is a result of the Sr segregation. The surface phase with a lower O 2p band would then have a lower concentration of oxygen vacancies, and thus, hinder the adsorption and incorporation of oxygen into the STF lattice. There is a large concentration of oxygen vacancies in bulk STF35 and STF100, as estimated by Jung and Tuller.[15] However, the availability of oxygen vacancies (Fig. 8(b)) and the free electrons particularly on the surface (Fig. 8(a)) can both be important for determining the oxygen reduction activity of the STF system.

The validity of the second mechanism depends on whether the segregated SrO_x surface phase behaves the same as in the bulk material systems, which Lee and Morgan considered in their model.[14] While we cannot prove this analogy from our current results, we do observe the change in the O 2p band in our measurements and the observed trends seem consistent with this model. Therefore, we cannot rule out the possible contribution of the O 2p band position in altering the surface reactivity on this material system. Nevertheless, this uncertainty may currently render the first mechanism[15] as more likely to govern the degradation of ORR activity on STF with increasing Fe content.

4. Conclusion

The influence of Sr segregation on the surface electronic structure and, ultimately, its impact on oxygen reduction kinetics, was investigated by coordinated AR-XPS, STM and STS studies on $SrTi_{1-x}Fe_xO_3$ dense thin films as a model cathode system. Sr segregation was found to increase with Fe content, consistent with previous findings. The origin of such a segregation could be related to the electrostatic and elastic interactions of Sr with the surrounding lattice in the bulk and on the surface.

The presence of the Sr segregation layer was found to have a profound impact on the surface electronic structure of STF films. While no energy gap was present on STF5 at 345 °C and 10^{-3} mbar of oxygen pressure (most probably due to the creation of defect states in the gap at high temperatures), STF35 and STF100 exhibited large band gaps on their surface and surprisingly, with that of STF100 greater than that of STF35. This trend in surface band gap is contrary to the previously reported results for the bulk band gap in STF that shows an opposite dependence on the Fe content. The increase in the surface band gap of STF with a larger Fe fraction is driven by a down-shift of the valence band top (and of the O 2p band) as a result of the formation of a more insulating Sr-rich surface layer. On the basis of surface chemistry deduced from AR-XPS analysis and the large band gap values measured by STS in this work, we conclude that the Sr segregation layer is more likely to be in the form of SrO_x on the surface of STF films. The electronic structure results demonstrate that such a SrO_x segregation layer on STF degrades the oxygen reduction kinetics through two possible mechanisms – (i) the surface layer acts as a charge transfer barrier and inhibits electron transfer from bulk STF to oxygen species adsorbed onto its surface and (ii) the down-shift of the O 2p band on the surface

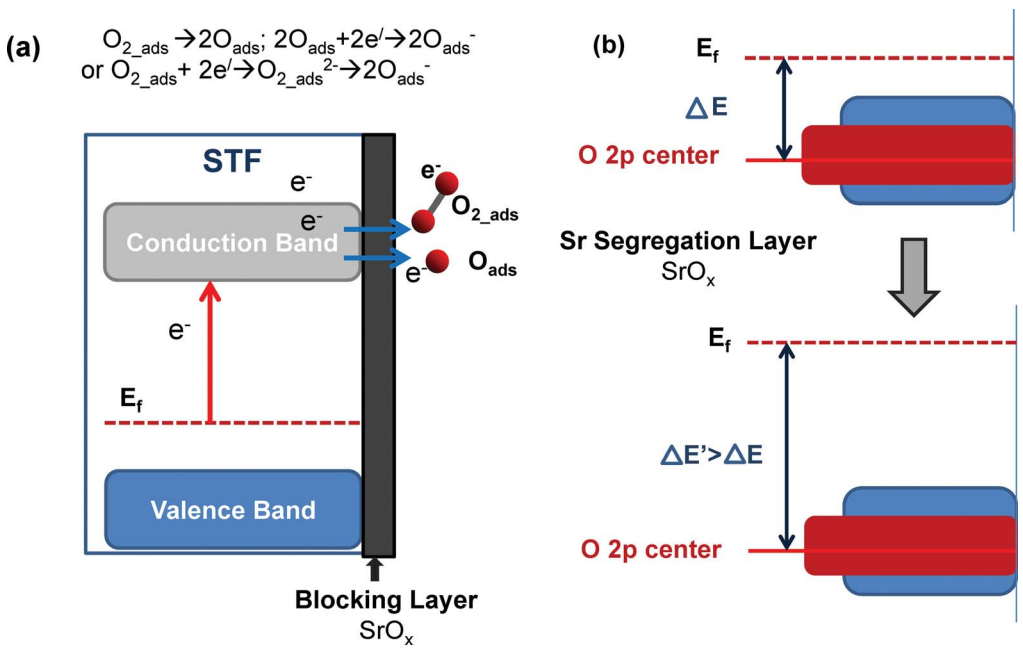

Fig. 8 Two possible mechanisms of how Sr segregation in the form of SrO_x on the surface impacts the oxygen reduction kinetics: (a) The Sr segregation layer, SrO_x, serves as a barrier layer that inhibits electron transfer from bulk STF to O_2 or O adsorbing onto the surface and (b) downshift in the O 2p position is associated with a more stable oxygen sub-lattice and consequently a smaller amount of oxygen vacancies are available on the surface for oxygen adsorption and incorporation into the lattice. The red box and the blue box represent the O 2p states and transition metal 3d states, respectively.

layer induces a smaller concentration of oxygen vacancies available for oxygen incorporation into the lattice. While these results were obtained on STF, the principal techniques, analysis and interpretations can be extended to other mixed conducting perovskite oxide cathodes to deduce the effect of surface electronic structure on ORR activity. A comprehensive understanding of these relationships offers the possibility of designing high-performance cathodes by tailoring their surface chemistry and electronic structure.

Acknowledgements

The authors thank Basic Energy Sciences, U.S. Department of Energy (contract # DE SC0002633) for their research support.

References

1 B. C. H. Steele and A. Heinzel, *Nature*, 2001, **414**, 345–352.
2 S. M. Haile, *Acta Mater.*, 2003, **51**, 5981–6000.
3 A. J. Jacobson, *Chem. Mater.*, 2010, **22**, 660–674.
4 S. B. Adler, *Chem. Rev.*, 2004, **104**, 4791–4843.
5 A. Chroneos, B. Yildiz, A. Tarancon, D. Parfitt and J. A. Kilner, *Energy Environ. Sci.*, 2011, **4**, 2774–2789.
6 B. Hammer and J. K. Norskov, *Nature*, 1995, **376**, 238–240.
7 R. A. De Souza and J. A. Kilner, *Solid State Ionics*, 1999, **126**, 153–161.
8 R. Merkle, J. Maier and H. J. M. Bouwmeester, *Angew. Chem., Int. Ed.*, 2004, **43**, 5069–5073.
9 K. Szot, M. Pawelczyk, J. Herion, C. Freiburg, J. Albers, R. Waser, J. Hulliger, J. Kwapulinski and J. Dec, *Appl. Phys. A: Mater. Sci. Process.*, 1996, **62**, 335–343.
10 T. T. Fister, D. D. Fong, J. A. Eastman, P. M. Baldo, M. J. Highland, P. H. Fuoss, K. R. Balasubramaniam, J. C. Meador and P. A. Salvador, *Appl. Phys. Lett.*, 2008, **93**, 151904.
11 C. N. Borca, B. Xu, T. Komesu, H. K. Jeong, M. T. Liu, S. H. Liou and P. A. Dowben, *Surf. Sci.*, 2002, **512**, L346–L352.
12 H. Dulli, E. W. Plummer, P. A. Dowben, J. Choi and S. H. Liou, *Appl. Phys. Lett.*, 2000, **77**, 570–572.
13 J. Suntivich, H. A. Gasteiger, N. Yabuuchi, H. Nakanishi, J. B. Goodenough and Y. Shao-Horn, *Nat. Chem.*, 2011, **3**, 546–550.
14 Y.-L. Lee, J. Kleis, J. Rossmeisl, Y. Shao-Horn and D. Morgan, *Energy Environ. Sci.*, 2011, **4**, 3966–3970.
15 W. Jung and H. L. Tuller, *Adv. Energy Mater.*, 2011, **1**, 1184–1191.
16 P. Decorse, G. Caboche and L. C. Dufour, *Solid State Ionics*, 1999, **117**, 161–169.
17 K. Katsiev, B. Yildiz, K. Balasubramaniam and P. A. Salvador, *Appl. Phys. Lett.*, 2009, **95**, 092106-1–092106-3.
18 W. Jung and H. L. Tuller, *Energy Environ. Sci.*, 2012, **5**, 5370–5378.
19 M. E. Lynch, L. Yang, W. T. Qin, J. J. Choi, M. F. Liu, K. Blinn and M. L. Liu, *Energy Environ. Sci.*, 2011, **4**, 2249–2258.
20 Y. Liang and D. A. Bonnell, *Surf. Sci.*, 1994, **310**, 128–134.
21 A. E. Bocquet, A. Fujimori, T. Mizokawa, T. Saitoh, H. Namatame, S. Suga, N. Kimizuka, Y. Takeda and M. Takano, *Phys. Rev. B: Condens. Matter Mater. Phys.*, 1992, **45**, 1561–1570.
22 M. P. de Jong, V. A. Dediu, C. Taliani and W. R. Salaneck, *J. Appl. Phys.*, 2003, **94**, 7292–7296.
23 H. Wei, W. Maus-Friedrichs, G. Lilienkamp, V. Kempter, J. Helmbold, K. Gomann and G. Borchardt, *J. Electroceram.*, 2002, **8**, 221–228.
24 P. A. W. van der Heide, Q. D. Jiang, Y. S. Kim and J. W. Rabalais, *Surf. Sci.*, 2001, **473**, 59–70.
25 J. Choi, H. Dulli, S. H. Liou, P. A. Dowben and M. A. Langell, *Phys. Status Solidi B*, 1999, **214**, 45–57.
26 M. Kubicek, A. Limbeck, T. Fromling, H. Hutter and J. Fleig, *J. Electrochem. Soc.*, 2011, **158**, B727–B734.
27 S. P. Jiang and J. G. Love, *Solid State Ionics*, 2001, **138**, 183–190.
28 E. Mutoro, E. J. Crumlin, M. D. Biegalski, H. M. Christen and Y. Shao-Horn, *Energy Environ. Sci.*, 2011, **4**, 3689–3696.
29 S. F. Wagner, C. Warnke, W. Menesklou, C. Argirusis, T. Damjanovic, G. Borchardt and E. Ivers-Tifee, *Solid State Ionics*, 2006, **177**, 1607–1612.
30 A. Rothschild, W. Menesklou, H. L. Tuller and E. Ivers-Tiffee, *Chem. Mater.*, 2006, **18**, 3651–3659.
31 W. Jung and H. L. Tuller, *J. Electrochem. Soc.*, 2008, **155**, B1194–B1201.
32 W. Jung and H. L. Tuller, *Solid State Ionics*, 2009, **180**, 843–847.
33 R. Merkle and J. Maier, *Phys. Chem. Chem. Phys.*, 2002, **4**, 4140–4148.
34 V. E. Alexandrov, J. Maier and R. A. Evarestov, *Phys. Rev. B: Condens. Matter Mater. Phys.*, 2008, **77**, 075111.
35 P. R. Watson, M. A. V. Hove and K. Hermann, *NIST Surface Structure Database – Version 5.0 National Institute of Standards and Technology*, Gaithersburg, MD, 2004.
36 K. Szot, W. Speier, J. Herion and C. Freiburg, *Appl. Phys. A: Mater. Sci. Process.*, 1997, **64**, 55–59.
37 H. Dulli, P. A. Dowben, S. H. Liou and E. W. Plummer, *Phys. Rev. B: Condens. Matter Mater. Phys.*, 2000, **62**, 14629–14632.
38 Y. Liang and D. A. Bonnell, *Surf. Sci.*, 1993, **285**, L510–L516.
39 S. N. Ruddlesden and P. Popper, *Acta Crystallogr.*, 1958, **11**, 54–55.
40 X. Guo, *Solid State Ionics*, 1995, **81**, 235–242.
41 H. B. Lee, F. B. Prinz and W. Cai, *Acta Mater.*, 2010, **58**, 2197–2206.
42 S. Estrade, J. M. Rebled, J. Arbiol, F. Peiro, I. C. Infante, G. Herranz, F. Sanchez, J. Fontcuberta, R. Cordoba, B. G. Mendis and A. L. Bleloch, *Appl. Phys. Lett.*, 2009, **95**, 072507.
43 A. Lussier, J. Dvorak, S. Stadler, J. Holroyd, M. Liberati, E. Arenholz, S. B. Ogale, T. Wu, T. Venkatesan and Y. U. Idzerda, *Thin Solid Films*, 2008, **516**, 880–884.
44 Z. Cai, M. Kubicek, J. Fleig and B. Yildiz, *Chem. Mater.*, 2012, **24**, 1116–1127.
45 J. C. Dupin, D. Gonbeau, P. Vinatier and A. Levasseur, *Phys. Chem. Chem. Phys.*, 2000, **2**, 1319–1324.
46 L. T. Hudson, R. L. Kurtz, S. W. Robey, D. Temple and R. L. Stockbauer, *Phys. Rev. B: Condens. Matter Mater. Phys.*, 1993, **47**, 10832–10838.
47 P. Liu, T. Kendelewicz, G. E. Gordon and G. A. Parks, *Surf. Sci.*, 1998, **412–413**, 287–314.
48 M. V. Ganduglia-Pirovano, A. Hofmann and J. Sauer, *Surf. Sci. Rep.*, 2007, **62**, 219–270.
49 T. Nishimura, A. Ikeda, H. Namba, T. Morishita and Y. Kido, *Surf. Sci.*, 1999, **421**, 273–278.
50 A. Hirata, A. Ando, K. Saiki and A. Koma, *Surf. Sci.*, 1994, **310**, 89–94.
51 Z. Cai, Y. Kuru, J. W. Han, Y. Chen and B. Yildiz, *J. Am. Chem. Soc.*, 2011, **133**, 17696–17704.
52 H. Bando, Y. Aiura, T. Shimizu, Y. Ochiai, Y. Haruyama and Y. Nishihara, *J. Electron Spectrosc. Relat. Phenom.*, 2001, **114**, 313–317.
53 A. Gunhold, L. Beuermann, M. Frerichs, V. Kempter, K. Gomann, G. Borchardt and W. Maus-Friedrichs, *Surf. Sci.*, 2003, **523**, 80–88.
54 H. Jalili, J. W. Han, Y. Kuru, Z. Cai and B. Yildiz, *J. Phys. Chem. Lett.*, 2011, **2**, 801–807.
55 G. P. Summers, *Phys. Rev. B: Condens. Matter Mater. Phys.*, 1979, **20**, 5275–5279.
56 M. Abbate, H. Ascolani, F. Prado and A. Caneiro, *Solid State Commun.*, 2004, **129**, 113–116.
57 J. Matsuno, Y. Okimoto, M. Kawasaki and Y. Tokura, *Phys. Rev. Lett.*, 2005, **95**, 76404.
58 P. Adler, A. F. Goncharov, K. Syassen and E. Schonherr, *Phys. Rev. B: Condens. Matter Mater. Phys.*, 1994, **50**, 11396–11402.
59 R. A. De Souza, *Phys. Chem. Chem. Phys.*, 2006, **8**, 890–897.

